



Fucoidan-based, tumor-activated nanoplatform for overcoming hypoxia and enhancing photodynamic therapy and antitumor immunity

Chu-Hung Chung^{a,b}, Kun-Ying Lu^{a,c}, Wei-Cheng Lee^{a,b}, Wen-Jing Hsu^{a,b}, Wen-Fu Lee^d, Jia-Zih Dai^{a,b}, Pei-Wei Shueng^{e,f}, Cheng-Wei Lin^{a,b,g,h,*}, Fwu-Long Mi^{a,b,c,**}

^a Department of Biochemistry and Molecular Cell Biology, School of Medicine, College of Medicine, Taipei Medical University, Taipei, Taiwan

^b Graduate Institute of Medical Sciences, College of Medicine, Taipei Medical University, Taipei, Taiwan

^c Graduate Institute of Nanomedicine and Medical Engineering, College of Medical Bioengineering, Taipei Medical University, Taipei, Taiwan

^d Department of Chemical Engineering and Biotechnology, Tatung University, Taipei, Taiwan

^e Division of Radiation Oncology, Far Eastern Memorial Hospital, New Taipei City, Taiwan

^f Faculty of Medicine, School of Medicine, National Yang-Ming University, Taipei, Taiwan

^g Center for Cell Therapy and Regeneration Medicine, Taipei Medical University, Taipei, Taiwan

^h Cell Physiology and Molecular Image Research Center, Wan Fang Hospital, Taipei Medical University, Taipei, Taiwan

ARTICLE INFO

Keywords:

Fucoidan

Hypoxia

Nanoparticle

Photodynamic therapy

Antitumor immunity

ABSTRACT

Multifunctional nanoplatforms combined with photodynamic therapy (PDT) and anticancer drugs have shown great promising in cancer therapy. However, their efficacy is limited by the low specificity, low oxygen levels, and a tolerant tumor immune microenvironment. Herein, we developed a biocompatible theranostic nanoplatform (FM@VP) based on co-assembly of a nanocomplex formed by a functional polysaccharide fucoidan and a bioreducible polyamidoamine (PAMAM) dendrimer, a photosensitizer verteporfin (VP), and MnO₂ nanoparticles (a tumor microenvironment responsive oxygen evolving nanomaterial) into a multifunctional nanoparticle cluster. The dendrimer-fucoidan polyionic nanocomplex (DFPN) specifically targeted P-selectin-overexpressed triple-negative breast cancer (TNBC) and the tumor-associated vasculature, and was sensitive to glutathione (GSH) in tumor. More importantly, this FM@VP nanocomplex simultaneously overcame tumor hypoxia, suppressed oncogenic signaling, and attenuated tumor-mediated immunosuppression, resulting in improving therapeutic efficacy of PDT while enhancing antitumor immunity and anti-metastasis. This discovery provides a powerful strategy for synergetic cancer targeting/photodynamic/immunotherapy and could serve as a safe clinical translational approach.

1. Introduction

Metastasis is the leading cause of cancer-related mortality, especially with triple-negative breast cancer (TNBC) which is the most lethal type of breast cancer. TNBC is characterized with high heterogeneity, an invasive nature, and a lack of treatment options. Moreover, patients frequently develop resistance to conventional chemotherapy or radiotherapy [1]. Eradication of TNBC is currently a critical unmet clinical need. Nanomedicine has emerged as an attractive anticancer strategy, and it has shown many advantages over conventional therapies and provides promising opportunities such as with imaging, diagnosis, drug

delivery, and improved cancer-targeted treatment. Photodynamic therapy (PDT) is one of the potential cancer treatments based on generating highly cytotoxic singlet oxygen (¹O₂) through interactions of a photosensitizer, light, and oxygen [2,3]. However, the hypoxic microenvironment of solid tumors is a major challenge and limitation for PDT [4]. Tumor hypoxia promotes aggressiveness, vascular angiogenesis, and resistance to various therapies [5]. PDT-evoked tumor hypoxia may even lead to cancer recurrence [6]. Therefore, overcoming tumor hypoxia by nanocarriers towards enhanced PDT [7–10]. Moreover, the overexpression of glutathione (GSH) in tumor cells can directly remove reactive oxygen species (ROS) to further reduce intracellular oxidative

* Corresponding author. Department of Biochemistry and Molecular Biology, School of Medicine, College of Medicine, Taipei Medical University, 250 Wu-Xing Street, Taipei, 11031, Taiwan.

** Corresponding author. Department of Biochemistry and Molecular Biology, School of Medicine, College of Medicine, Taipei Medical University, 250 Wu-Xing Street, Taipei, 11031, Taiwan.

E-mail addresses: cwlin@tmu.edu.tw (C.-W. Lin), flmi530326@tmu.edu.tw (F.-L. Mi).

<https://doi.org/10.1016/j.biomaterials.2020.120227>

Received 26 March 2020; Received in revised form 17 June 2020; Accepted 6 July 2020

Available online 10 July 2020

0142-9612/© 2020 Elsevier Ltd. All rights reserved.

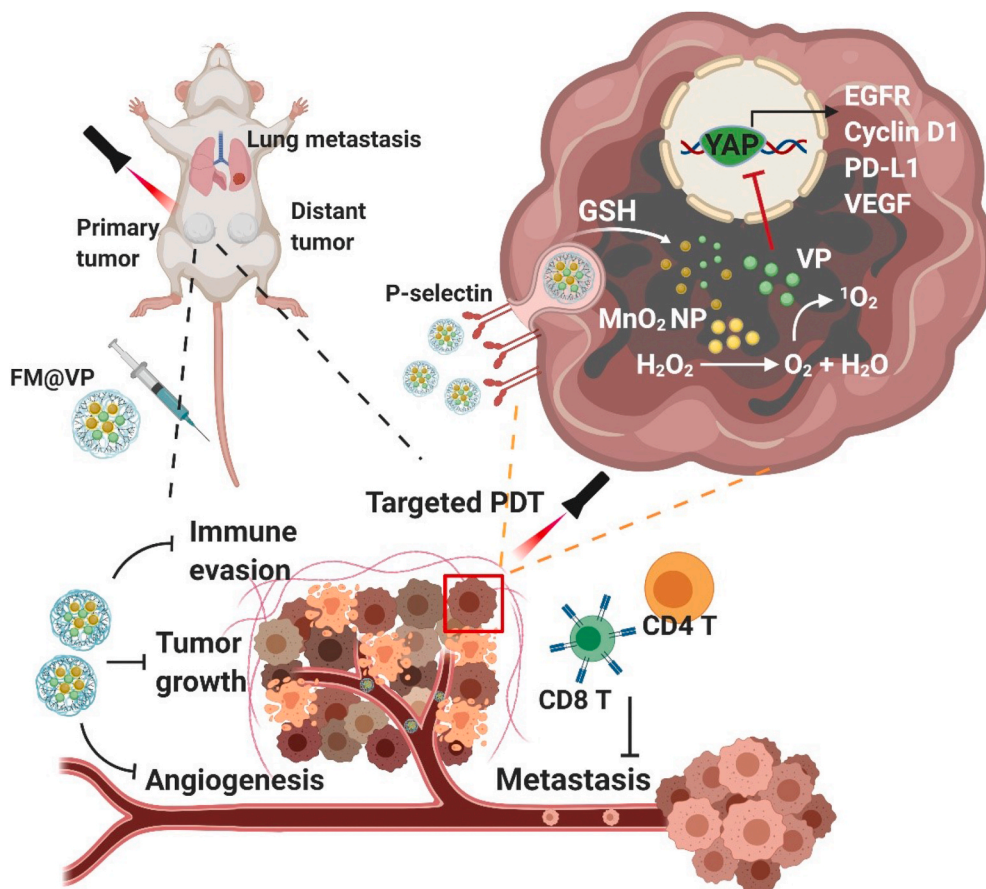
stress [11]. The generation of ROS is more toxic towards normal cells due to their lower GSH levels, which results in increased side effects of PDT [12].

In addition to the production of ROS by PDT, the secretion or exposure of damage-associated molecular patterns (DAMPs) from PDT-elicited damage to cells may trigger the host immune system, including activation of T cells and dendritic cells. Several studies investigated the involvement of immune modulation with PDT [13–15]. However, the presence of immune checkpoint molecules such as programmed death-protein 1 (PD1), programmed death-ligand 1 (PD-L1), and cytotoxic T lymphocyte-associated antigen 4 (CTLA4), in tumor cells limits the activation and effective functioning of antigen-reactive T cells and enables tumors to escape from immune elimination [16]. Overcoming tumor-mediated immunosuppression by nanocarriers via a combination or conjugation with immune checkpoint inhibitors would offer the possibility of amplifying antitumor immune responses and improving therapeutic efficacies [17–19]. Other studies focused on regulating the tumor immune microenvironment by nanomedicine [20, 21]. Thus, it would be highly desirable to develop an efficient tumor-activated nanoplatform compatible with antitumor immunity to achieve therapeutic feasibility.

On this basis, the present study attempted to develop a nanoplatform which is able to achieve the above-mentioned goals. Benefiting from the high catalytic efficiency of MnO_2 with overexpressed H_2O_2 in the tumor microenvironment (TME), MnO_2 nanoparticles (NPs) can generate O_2 to modulate tumor hypoxia and enhance the effect of PDT. Nanoparticles are typically stabilized by electrostatic or steric repulsion, and they can co-assemble with polymers or small molecules into clusters under a variety of external triggers [22]. Dendrimers shows host-guest chemical properties because the hydrophilic functional groups on the exterior surface enhance their water solubility, but the inner core and branches

are responsible for improving the solubility of hydrophobic drugs. Dendrimers can be used as a template for modulating the synthesis of nanoparticles and clusters and can serve as ligands to increase their stability [23]. Dendrimer-cluster multivalent interactions prevent the clusters from aggregating or being leached out [24]. Guest-functionalized dendrimers play a key role in the self-assembly of inorganic NPs into supramolecular NP clusters because of host-guest and electrostatic interactions formed between the NPs [25].

Herein, we developed a smart theranostic FM@VP nanoplatform with fucoidan which has the ability to target P-selectin-positive breast cancer cells and the tumor-associated vasculature [26]. The FM@VP nanoplatform was constructed based on the co-assembly of the photosensitizer, verteporfin (VP), and MnO_2 NPs with a bioreducible, polyamidoamine (PAMAM) dendrimer through the formation of dendrimer-VP hydrophobic interactions and N–Mn bonds on surface Mn sites of MnO_2 , in association with a dendrimer-fucoidan polyionic nanocomplex (DFPN) to form nanoparticle clusters. The VP- and MnO_2 -loaded nanoparticle clusters were sensitive to glutathione (GSH). Given that tumor cells have higher levels of GSH compared to normal tissues, rapid disintegration of the clusters occurred as a consequence of reducing the disulfide bounds in the dendrimers to further have the ability to selectively “turn on” fluorescence. Subsequently, the release of VP enhanced PDT and alleviated tumor hypoxia with the assistance of oxygen supplied by the MnO_2 NPs. Moreover, VP not only elicited PDT but also synergistically suppressed oncogenic signaling and attenuated tumor-mediated immunosuppression through its inhibition on yes-associated protein (YAP). This nanoplatform exhibits multifunctional characteristics including selective cancer-targeting/photodynamic/immunotherapy, as a result of enhancing antitumor growth and preventing secondary tumor formation in distant organs (Scheme 1). This is the first research to provide proof of concept that a smart, biocompatible fucoidan-based nanoplatform can



Scheme 1. Illustration of the theranostic FM@VP nanoplatform for overcoming tumor hypoxia and enhancing the photodynamic efficacy in breast cancer. The FM@VP nanocomplex exhibited targeting ability by fucoidan for P-selectin-positive TNBC and the tumor-associated vasculature. VP- and MnO_2 -loaded nanoparticle clusters were sensitive to glutathione (GSH) of tumor cells due to the disulfide bound-linked dendrimer. Subsequently, the release of VP enhanced PDT and alleviated tumor hypoxia with the assistance of oxygen supplied by MnO_2 NPs. Moreover, VP not only accentuated PDT but also synergistically suppressed oncogenic signaling, inhibited tumor angiogenesis, and attenuated tumor-mediated immunosuppression, as a result of enhancing the therapeutic efficacy of PDT and further prevented secondary tumor formation in metastatic organs.

empower sweeping antitumor function. This powerful strategy can serve a safe clinical translational approach in cancer-targeted therapy.

2. Results and discussion

2.1. Preparation and characterization of the FM@VP nanoformulation

Due to the hydrophobic nature of the inner core and branches, dendrimers play an important role in the loading and delivery of hydrophobic drugs [27]. The dendrimer also acts as a ligand to increase the stability of nanoparticles and clusters [22–24]. Therefore, in the present study, a bioreducible, polyamidoamine (PAMAM) dendrimer was used as a nanocarrier for the co-delivery of VP, a hydrophobic photosensitizer, and MnO₂ NPs. Nevertheless, a high positive charge can increase the cytotoxicity of dendrimers. In addition, dendrimers without modification with ligands cannot actively target tumors. Fucoidan is a fucose-based, sulfated polysaccharide derived from brown algae, which was reported to target P-selectin-overexpressing tumor cells [26,28]. Our previous studies have reported the development of fucoidan-based nanocarriers for oral drug delivery and antibacterial application [29–32]. The molecular weight of fucoidan used in this study was 8775 Da as determined by Gel Permeation Chromatography (GPC Analysis),

which was obtained by hydrolysis of crude fucoidan with H₂O₂ through breaking glycosidic bonds [33,34]. The molecular weight of the bioreducible PAMAM dendrimer was 1522 Da, as indicated by the NMR identification of the synthesized compound (Supplemental Materials and Methods 1). Therefore, fucoidan and dendrimer were easily to form nanocomplex and thus the positively charged dendrimer was modified with the negatively charged polysaccharide, fucoidan, to increase its biocompatibility and tumor-targeting ability.

Dendrimers are generally of small sizes (3–10 nm) and thus are easily removed through extravasation and renal clearance. Modifying dendrimers with polymers can increase their size, which not only increases their circulation in the blood but also improves their antitumor efficacy [35,36]. We first found that fucoidan and a bioreducible PAMAM dendrimer formed a polyionic nanocomplex (DFPN) through electrostatic interactions upon direct mixing of these oppositely charged compounds in water. The addition of dendrimer to fucoidan solution resulted in an increase in turbidity and the transmittance of fucoidan solution decreased with the increase of dendrimer-to-fucoidan weight ratio, revealing the formation of self-assembled DFPN nanocomplex (Supplemental Fig. S1A). The DFPN-based nanocomplex was further prepared by co-assembly of the photosensitizer, VP, and MnO₂ NPs to obtain a tumor-targeting and oxygen-boosting nanoplatform for enhanced

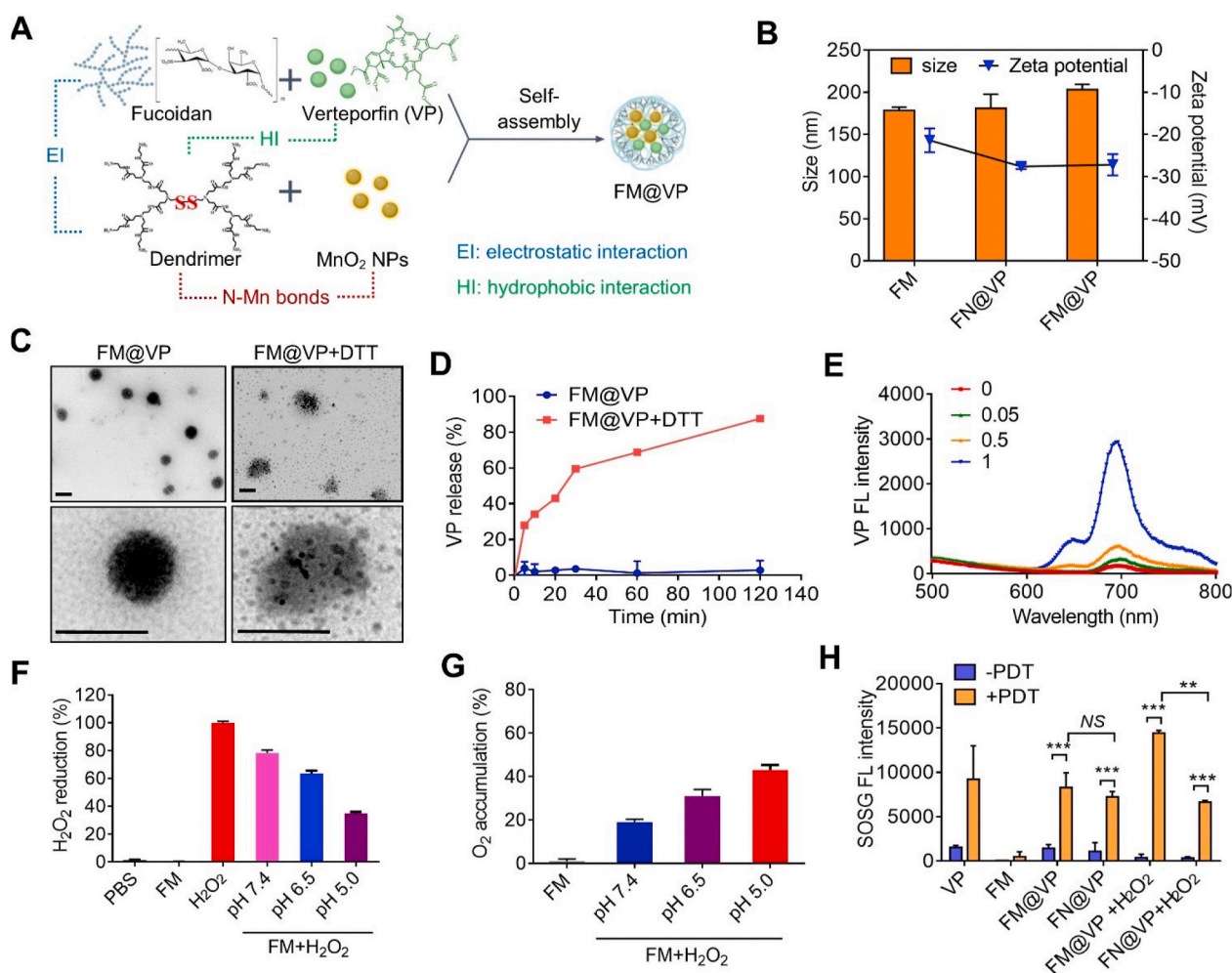


Fig. 1. Characterization of FM@VP. (A) FM@VP nanoparticle cluster assembling scheme. (B) Z-average diameter and surface zeta potential of FM, FN@VP, and FM@VP nanoformulations. (C) TEM images of FM@VP nanoparticle cluster with and without DTT treatment. Scale bar = 200 nm. (D) In vitro release of VP from FM@VP nanoparticle clusters was dependent on disulfide bond reduction. (E) Response of the VP fluorescent intensity of FM@VP nanoparticle cluster to stimuli in the presence of DTT (0, 0.05, 0.5, and 1 M). (F) Determination of H₂O₂ decomposition and (G) oxygen generation by FM nanocomplex. Data are presented as percentage relative to the control group. The raw spectrums are shown in Supplemental Figure S5 (H) Fluorescent intensity of SOSG by FM, FN@VP, and FM@VP nanoformulations with or without light irradiation (1.1 W/cm², 690 nm). Data are presented as the mean ± SD. **p < 0.01, ***p < 0.001, assessed using an unpaired t-test.

photodynamic efficiency. To improve the loading efficiency of VP and MnO₂ NPs, VP was mixed with fucoidan aqueous solution and MnO₂ NPs was mixed with dendrimer aqueous solution, separately. Dendrimer can serve as a ligand to coordinate with MnO₂ NPs through the formation of N–Mn bonds on surface Mn sites and thus helps to prevent loss of MnO₂ NPs during the co-assembly process for forming FM@VP nanocomplex. Fucoidan is a biological macromolecule which can serve as a solubilizer to improve the solubility of VP in aqueous solution and thus can reduce the usage amount of solvent (DMSO). Dendrimers have hydrophilic functional groups on the exterior surface but hydrophobic inner core and branches. The hydrophobic interactions between dendrimer and VP can cause the formation of dendrimer-VP nanocomplex prior to the co-assembly process when dendrimer and VP are directly mixed, which can hinder the interactions between dendrimer and fucoidan (Fig. 1A).

Three different DFPN formulations, including FM (with MnO₂ loading), FN@VP (with VP loading), and FM@VP (with MnO₂/VP loading) exhibited good colloidal stability in water and serum-containing medium for at least 8 h (Supplemental Figs. S1B–C). The hydrodynamic sizes of the FM, FN@VP, and FM@VP nanofomulations were 178 ± 4.0 , 181 ± 16.5 , and 206 ± 6.2 nm (Fig. 1B). Polydispersity index (PDI) values of the FM, FN@VP, and FM@VP nanofomulations were 0.15 ± 0.02 , 0.19 ± 0.05 , and 0.23 ± 0.05 , respectively (Supplemental Fig. S1B). Zeta potentials of the FM, FN@VP, and FM@VP nanofomulations were -21 ± 2.8 , -27 ± 0.6 , and -27 ± 2.3 mV, respectively (Fig. 1B), suggesting that the nanofomulation samples were covered with fucoidan. Moreover, the absorption spectrum of the FM@VP nanofomulation showed a strong absorption band at 700 nm, which was assigned to the characteristic absorption of VP. The encapsulation efficiency of VP calculated using the absorption spectrum was approximately 90% (Supplemental Fig. S1E).

Next, the Fourier transformation infrared (FTIR) spectra of DFPN and the FM@VP nanofomulation were examined. The bands at 1680 and 1540 cm⁻¹ were assigned to amide I and II, and primary amine of the bioreducible PAMAM dendrimer. Characteristic peaks of O=S=O vibration (1255 cm⁻¹) and C–O–S stretching (850 cm⁻¹) were assigned to the sulfate groups of fucoidan (sulfated fucose residues). DFPN showed the characteristic peaks of dendrimer (1540 cm⁻¹) and fucoidan (1255 cm⁻¹) but the intensity of the band at 1540 cm⁻¹ decreased with the increase of fucoidan-to-dendrimer weight ratio. The spectrum of FM@VP (fucoidan/dendrimer = 10:1) consisted mostly of the characteristic absorption bands of fucoidan, revealing the abundance of fucoidan in the nanofomulation (Supplemental Fig. S2). In addition, the diffraction patterns of MnO₂ NPs and FM@VP nanofomulation were determined by X-ray diffraction (XRD). Results showed that the XRD pattern of the FM@VP nanofomulation matched well with the pattern of MnO₂ NPs, further indicating the incorporation of MnO₂ NPs in the FM@VP nanofomulation (Supplemental Fig. S3). The encapsulation efficiency of MnO₂ NPs in FM@VP was 74.8% as determined by ICP-OES. Additionally, the absorption spectra from the centrifuged supernatant of the FM@VP nanocomplex didn't show the absorption band of MnO₂ NPs (Supplemental Fig. S4A), confirming that MnO₂ NPs were successfully assembled and encapsulated in the nanocomplex. Moreover, transmission electron microscopic (TEM) images illustrating the FM@VP nanocomplex showed co-assembled VP/MnO₂ DFPN clusters with a particle size of around 200 nm (Fig. 1C). These data indicated the successful combination of fucoidan with the dendrimer to form the DFPN and the co-assembly of VP and MnO₂ with the DFPN into FM@VP nanoclusters. TEM images also showed that the FM@VP nanoclusters had completely disintegrated in the presence of the disulfide-reducing agent, dithiothreitol (DTT), because the disulfide bonds in the dendrimer were rapidly cleaved by DTT via a thiol-disulfide exchange reaction [37] (Fig. 1C). The responsiveness of the nanoparticle cluster formulations to stimuli was further confirmed by the increased particle size because of disassembly of the nanoparticle cluster (Supplemental Fig. S1C). These data indicated that the DFPN clusters had a redox-responsive property, and were sensitive to a reduction in disulfide

bonds. Subsequently, the redox-sensitive release property of the FM@VP nanoparticle clusters was investigated in the presence of DTT. As anticipated, the release of VP was rapidly detected within 10 min after the addition of DTT, and it continued to be released until it had reached 90% by 120 min of incubation (Fig. 1D). Additionally, the VP fluorescent signal was almost completely quenched after formation of the FM@VP nanoparticle clusters, which was ascribed to hydrophobic interactions between the dendrimer and VP molecules and π – π stacking interactions between VP's own porphyrin rings [38]. Fig. 1E shows that the FM@VP nanoparticle clusters were able to restore VP's fluorescence in the presence of DTT in a dose-dependent manner, indicating disintegration of the FM@VP nanoparticle clusters through redox-responsive cleavage of the GSH-reducible linker (disulfide bonds) in the dendrimer. Disassembly of FM@VP nanoparticle clusters was attributed to cleavage of the bioreducible linker (disulfide bond) in the dendrimer by DTT, simultaneously resulted in fluorescence recovery. The initial "turning-off" and then the final "turning-on" of fluorescence would be beneficial for reducing phototoxic effects in normal tissues and for the instantaneous visual sensing of tumors.

PDT can trigger tumor cells death by producing ¹O₂; however, hypoxia in the tumor microenvironment leads to the acidic tumor microenvironment and generate excessive amounts of H₂O₂. In view of the fact that MnO₂ catalyzes the decomposition of H₂O₂ to oxygen, MnO₂ NPs incorporated in FM@VP nanoparticle clusters can have the potential to relieve tumor hypoxia. The results of ICP-OES showed that MnO₂ NPs did not release from FM@VP nanoparticle clusters in the absence of DTT. However, DTT significantly triggered rapid and efficient release of MnO₂ NPs from FM@VP nanoparticle clusters. More than 90% of incorporated MnO₂ NPs were released within 2 h under the reducing condition (Supplemental Fig. S4B), further confirming the redox-responsive characteristic of FM@VP nanoparticle clusters.

The catalyzed reaction of H₂O₂ by MnO₂ reacts more rapidly in the presence of H⁺ (i.e. hypoxic conditions) [39]; therefore, the effect of FM@VP nanoparticle clusters on decomposition of H₂O₂ and generation of oxygen were studied under different pH conditions. Fig. 1F showed that the absorbance of the ferric-xylenol orange complex at 560 nm, which correlated with the concentration of H₂O₂, decreased by the addition of FM@VP nanoparticle clusters to H₂O₂. The decomposition of H₂O₂ was accelerated under acidic conditions, such as pH 6.5 (tumor microenvironment pH) and 5.0 (lysosome pH). After 1 h of reaction, the remaining ratio of H₂O₂ decreased from 90% to 65% along with the decrease of pH value from 7.4 to 5.0 (Fig. 1F and Supplemental Fig. S5A). Moreover, the degradation of H₂O₂ by FM@VP nanoparticle clusters could generate oxygen as evidenced by the fluorescence emission from an oxygen sensor (Fig. 1G and Supplemental Fig. S5B). In contrast to the remaining ratio of H₂O₂, the level of oxygen generated at pH 6.5 and 5.0 were 1.7- folds and 3.5-folds higher than that generated at 7.4, implying that the FM@VP nanoparticle clusters could be used as an ideal oxygen self-sufficient nanopatform to overcome tumor hypoxia for PDT.

The ¹O₂ generation ability of FM@VP nanoparticle clusters was then examined using singlet oxygen sensor green reagent (SOSG) as an indicator [40]. Under irradiation, the ¹O₂ generated by FM@VP nanoparticle clusters (with the combination of photosensitizer VP and MnO₂ NPs) in the presence of H₂O₂ caused the highest fluorescence enhancement of SOSG among all groups (Fig. 1H), indicating that ¹O₂ generated by this system was greatly improved by H₂O₂. In contrast, ¹O₂ generated by the nanoparticle clusters lacking MnO₂ NPs (FN@VP) was not significantly enhanced after exposure to light irradiation even in the presence of H₂O₂. The results suggested that the MnO₂ NPs incorporated in FM@VP nanoparticle clusters was effective in improving the ¹O₂ generation capability of VP, allowing for the promotion of PDT efficiency by relieving tumor hypoxia with the existence of H₂O₂.

2.2. FM@VP targets P-selectin-positive TNBC

To evaluate the binding specificity of the FM@VP nanoparticle clusters on tumor cells, we compared TNBC MDA-MB-231 cells and 3T3-L1 fibroblasts in response to the presence of FM@VP. As shown in Fig. 2A, VP fluorescent emission significantly increased in FM@VP-treated MDA-MB-231 cells, compared to that in 3T3-L1 cells (Fig. 2A, left panel). These data support the notion of high GSH levels in cancer cells and also confirm the capability of tumor-activated drug release by the FM@VP. We next evaluated the cellular uptake capacity of free VP and FM@VP nanoparticle clusters in MDA-MB-231 cells, and results showed that the ability of cells to take up FM@VP nanoparticle clusters was 2.5-fold greater than that of free VP, whereas the uptake of FM@VP in MDA-MB-231 cells was abolished by pretreatment with fucoidan (Fig. 2A, right panel), confirming that fucoidan-based DFPN clusters enhanced drug delivery to tumor cells.

Next, we evaluated the anticancer capacity of FM@VP nanoparticle clusters in MDA-MB-231, MDA-MB-468, and HCC1806 TNBC cells. Results of the cell viability assay showed that FM@VP exhibited the greatest growth inhibition in MDA-MB-231 and MDA-MB-468 cells, compared to free VP and the FM (without VP loading)-treated groups

(Fig. 2B and Supplemental Fig. S6A). The FM nanocomplex showed no obvious inhibitory activity against tumor cells (Supplemental Fig. S6A). We further treated TNBC cells with light irradiation, and results showed that the cell viability significantly decreased in FM@VP treatment combined with light irradiation, compared to cells treated with free VP or free VP plus light irradiation (Fig. 2B). However, the cytotoxicity of FM@VP against HCC1806 cells was no different, despite light irradiation increasing the cytotoxicity in both the free VP and FM@VP groups (Supplemental Fig. S6B). Because fucoidan was reported to target P-selectin, we hypothesized that the specificity of FM@VP nanoparticle clusters against TNBC cells might depend on the presence of P-selectin. As we expected, the level of P-selectin (*SELP*) was upregulated in MDA-MB-231 and MDA-MB-468 cells, compared to that in HCC1806 cells (Fig. 2C). Furthermore, results of the calcein-AM/propidium iodide (PI) staining assay indicated that cell death was triggered by the FN@VP and FM@VP nanocomplexes, while all cancer cells were killed when FM@VP were combined with light irradiation (Fig. 2D). On the contrary, the FM nanocomplex showed less cytotoxicity, both with and without light irradiation (Fig. 2D). Moreover, light irradiation rapidly induced intracellular ROS accumulation by FN@VP and FM@VP-treated cells, compared to FM-treated cells (Fig. 2E), indicating that the

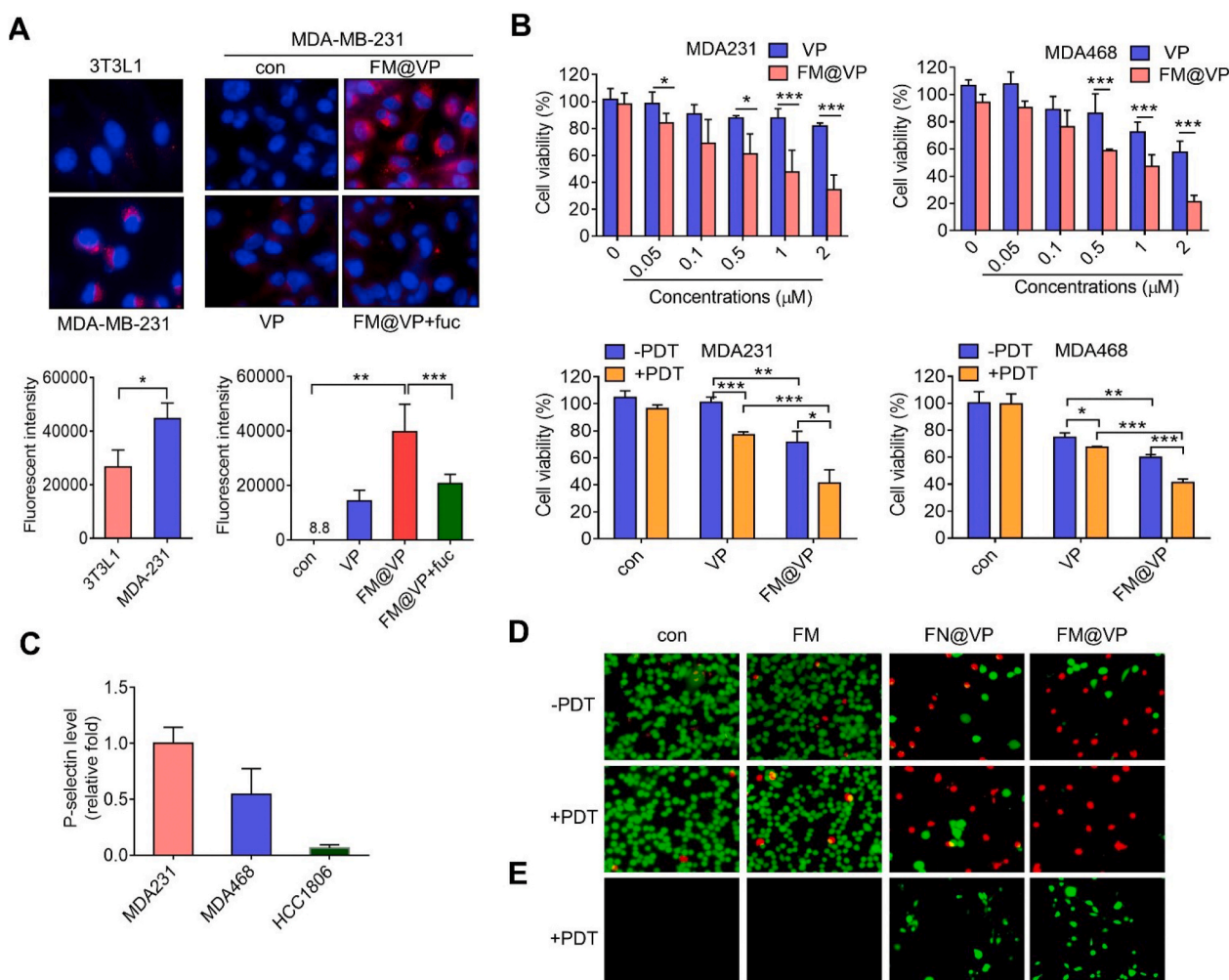


Fig. 2. Selectivity and phototoxicity of FM@VP nanocomplex. (A) Deconvolution fluorescent images of cellular uptake of FM@VP in 3T3L1 and MDA-MB-231 cells (left panel), and in the presence of free fucoidan (right panel). Intracellular fluorescent intensity of VP was quantified with a fluorescent spectrometer. (B) Cellular viability of TNBC cells treated with free VP and FM@VP, with and without light irradiation. (C) Relative expression of P-selectin (*SELP*) mRNA by TNBC cells. (D) Calcein-AM/propidium iodide (PI) staining of live and dead MDA-MB-231 cells after treatment with FM, FN@VP, and FM@VP, with and without light irradiation. (E) Representative images of intracellular ROS accumulation in MDA-MB-231 cells treated with FM, FN@VP, and FM@VP combined with light irradiation. Data are presented as the mean \pm SD. * $p < 0.05$; ** $p < 0.01$; *** $p < 0.001$, assessed using an unpaired *t*-test.

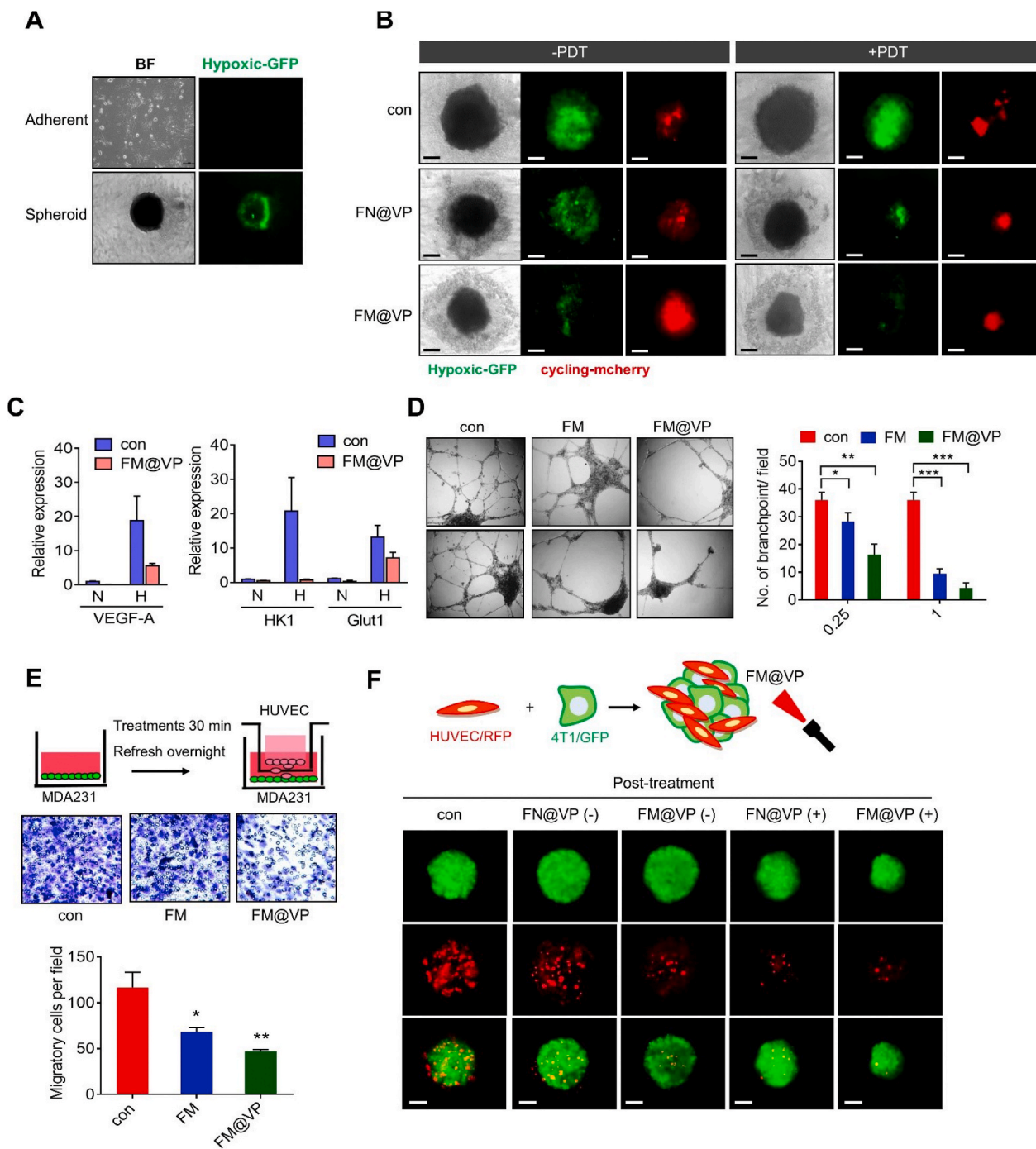


Fig. 3. Enhanced inhibitory capacity against tumor hypoxia and angiogenesis by FM@VP nanocomplex. (A) 4T1/hypoxCR cells were cultured in an adherent or spheroid condition for 48 h. GFP-positive hypoxic tumor cells were observed under an inverted fluorescent microscope. BF, bright field. (B) FM@VP alleviated hypoxia and enhanced PDT efficacy in 4T1/hypoxCR tumorspheres. Fluorescent microscopic images of GFP-positive hypoxic tumor cells and mcherry-positive proliferating cells in 4T1/hypoxCR tumorspheres were treated with FN@VP or FM@VP in the presence or absence of light irradiation. BF, bright field. Bar, 100 μ m. (C) Suppression of hypoxia-induced gene expressions by FM@VP, as determined by a real-time PCR analysis. (D) Light microscopic images of tube formation of HUVECs treated with FM or FM@VP nanoformulations. Quantitative data indicate the number of branch points. (E) Schematic diagram of transwell migration of HUVECs cocultured with FM- or FM@VP-treated MDA-MB-231 cells (upper panel). Representative images (middle panel) and quantitative data (lower panel) of migrated HUVECs are shown. (F) Schematic diagram of a 3D coculture model of HUVECs/RFP and 4T1/GFP tumorspheres treated with FN@VP or FM@VP in the presence or absence of light irradiation. Representative fluorescent images are shown. Bar, 100 μ m. Data are presented as the mean \pm SD. * p < 0.05; ** p < 0.01; *** p < 0.001, assessed using an unpaired t -test.

encapsulation of VP is responsible for ROS elicitation. These data together show the good binding specificity of FM@VP nanoparticle clusters to P-selectin-positive TNBC cells.

2.3. FM@VP overcome tumor hypoxia, thereby rendering a therapeutic advantage for PDT

Tumor hypoxia is an important impediment for effective PDT. In order to evaluate the encapsulation of MnO₂ NPs into the FM@VP nanoparticle clusters with the ability to overcome tumor hypoxia and produce therapeutic advantage for PDT, we cultured 4T1/hypoxCR cells which expressed the green fluorescent protein (GFP) in response to hypoxic conditions and mcherry in cycling cells, respectively. 4T1/hypoxCR cells were cultured into tumorspheres, and we detected that GFP-positive cells were increased in tumorspheres after 48 h of incubation, compared to the adherent cells (Fig. 3A). The hypoxic tumor region in the tumorspheres increased through 96 h of incubation (Supplemental Fig. S7A). On the contrary, the number of proliferating cells gradually decreased in 4T1/hypoxCR tumorspheres (Supplemental Fig. S7A), consistent with previous findings that cell division is down-regulated during hypoxia [41]. Importantly, tumorspheres treated with FN@VP slightly decreased the hypoxic tumor area, whereas treatment with FM@VP robustly diminished the formation of hypoxic tumor cells (Fig. 3B). We also observed that the decrease in tumor hypoxia by FM@VP was accompanied by an increase in proliferating cells (Fig. 3B), while treatment of tumorspheres with FM@VP combined with light irradiation reduced hypoxia of the tumor and also inhibited tumor proliferation (Fig. 3B). These data indicated that the reduction of the hypoxia of the tumorspheres by FM@VP resulted in enhanced PDT efficacy. We also stained MDA-MB-231 tumorsphere with a hypoxic probe, and consistent results were obtained that tumor hypoxia was elevated at 96 h by the formation of tumorspheres (Supplemental Fig. S7B). Moreover, MDA-MB-231 cells failed to form tumorspheres with either pretreatment or post-treatment with FM@VP plus light irradiation (Supplemental Fig. S7C), and pretreatment with FM@VP diminished the expression of hypoxia-related markers, including vascular endothelial growth factor (VEGF), glucose transporter 1 (Glut1), and hexokinase 1 (HK1) (Fig. 3C).

2.4. Suppression of tumor-elicited angiogenesis

Tumor hypoxia-elicited angiogenesis plays an important role in tumor growth and metastasis. To further examine the inhibitory activity of FM@VP nanoparticle clusters on tumor angiogenesis, we treated human umbilical vascular endothelial cells (HUVECs) with FM@VP. As shown in Fig. 3D, FM@VP encapsulating 0.25 μM VP suppressed formation of capillary-like structures in HUVECs, whereas FM nanocomplexes without VP encapsulation showed less of an effect on tube formation, indicating that VP is responsible for exerting the anti-angiogenic activity of FM@VP nanoparticles. Interestingly, higher concentrations of FM nanocomplexes exhibited inhibitory activity against tube formation (Fig. 3D). These data were similar to those of previous studies in which fucoidan attenuated tumor angiogenesis [42, 43]. Notably, encapsulation of 1 μM VP in FM@VP drastically suppressed tube formation in HUVECs (Fig. 3D). We further tested the effect of FM nanocomplexes on tumor-elicited angiogenesis. As shown in Fig. 3E, pretreatment with FM@VP, but not FM nanocomplexes, significantly suppressed tumor-induced endothelial cell migration (Fig. 3E). Moreover, we applied a 3D co-culture of 4T1/GFP spheroids with HUVEC/red fluorescent protein (RFP) to construct tumor-associated vascularization *in vitro*, and we evaluated the efficacy of PDT with FM@VP. As shown in Figs. 3F and 4T1/GFP cells induced differentiation and elongation of HUVECs/RFP in spheroidal tumors, and treatment with FN@VP had a minor effect on vascular formation in tumorspheres. However, treatment with FM@VP effectively decreased the growth of endothelial cells. Notably, FM@VP combined with light

irradiation drastically suppressed vessel formation and induced tumor-sphere regression (Fig. 3F). Additionally, pretreatment of 4T1/GFP cells with FM@VP robustly impeded the growth of tumors and endothelial cells both with and without light irradiation (Supplemental Fig. S8). Together, these data highlighted that the FM@VP nanocomplex possesses the ability to simultaneously decrease hypoxic tumor-elicited pro-angiogenesis and overcome the hypoxia-dampened efficacy of PDT. Moreover, FM@VP could further prevent tumor-associated vasculature formation.

2.5. A dual inhibitory effect on targeted therapy and antitumor immunity via suppressing YAP signaling

It was reported that VP inhibits tumor growth by attenuating the Hippo-YAP signaling cascade. We previously identified that YAP regulated the EGFR in lung cancer cells and promoted glycolysis in colon cancer cells [44,45], and overexpression of YAP was associated with cancer stemness and poor prognoses in TNBC [46]. To further investigate the targeted-therapeutic efficacy of FM@VP, we treated MDA-MB-231 cells with different concentrations of FM@VP. Results showed that FM@VP dose-dependently inhibited protein levels of YAP, which was accompanied by decreases in YAP downstream molecules including CTGF, cyclin D1, and EGFR (Supplemental Fig. S9A). Consistent results were obtained in free VP-treated MDA-MB-231 cells (Supplemental Fig. S9B). On the contrary, treatment with the FM nanocomplex showed no inhibitory activity against either YAP or YAP downstream targets (Supplemental Fig. S9A). These data indicated that the encapsulation of VP in FM@VP was obligatory for targeted therapy for TNBC.

We further exploited FM@VP-induced anticancer signaling in MDA-MB-231 cells. A whole-transcriptome analysis revealed that 1703 downregulated and 1203 upregulated genes were significantly affected by FM@VP (Supplemental Fig. S10A). Among them, we found that signaling pathways, including PI3K-AKT, Rap1, and transforming growth factor (TGF)-β, were significantly affected by FM@VP (Fig. 4A). Of note, Hippo signaling was attenuated by FM@VP as well (Fig. 4A). Furthermore, an ingenuity pathway analysis (IPA) depicted that several mitogenic signaling pathways, including STAT3, NFκB, and Wnt/β-catenin, were significantly affected by FM@VP (Fig. 4B, Supplemental Figs. S10B) and a functional annotation analysis also revealed that cellular movement, growth, differentiation, and immune trafficking were involved in response to FM@VP (Fig. 4C). We further validated that FM@VP but not FM nanocomplexes suppressed downstream molecules of YAP (Fig. 4D). These data suggest that FM@VP not only displays PDT activity but also possesses the ability to suppress oncogenic signaling in TNBC.

2.6. FM@VP suppresses PD-L1 and induces T cell-elicited tumoricidal activity

Recent studies reported that the immune checkpoint molecule, PD-L1, is regulated by YAP/TAZ [47,48]. It was reported that PD-L1 expression in tumors and host antigen-presenting cells was associated with tumor immune evasion and poor clinical outcomes [49]. Blockage of PD-L1/PD-1 by either a monoclonal antibody or small-molecule inhibitors is a promising therapeutic approach. Therefore, we further investigated the effect of FM@VP and the FM nanocomplexes on PD-L1. We found that treatment with VP robustly downregulated the PD-L1 protein level (Supplemental Fig. S9C). Surprisingly, we found that individual treatment with both FM@VP or the FM nanocomplex suppressed PD-L1 (Fig. 4E, Supplemental Fig. S9D); nevertheless, FM@VP exhibited greater inhibitory activity on PD-L1 compared to the FM-treated group (Fig. 4E, Supplemental Fig. S9D). Considering the pivotal role of PD-L1 in tumor immune evasion, we sought to evaluate T cell-mediated cytotoxicity toward TNBC cells. MDA-MB-231/GFP cells were pretreated with FM@VP (encapsulating 1 μM VP) and the FM

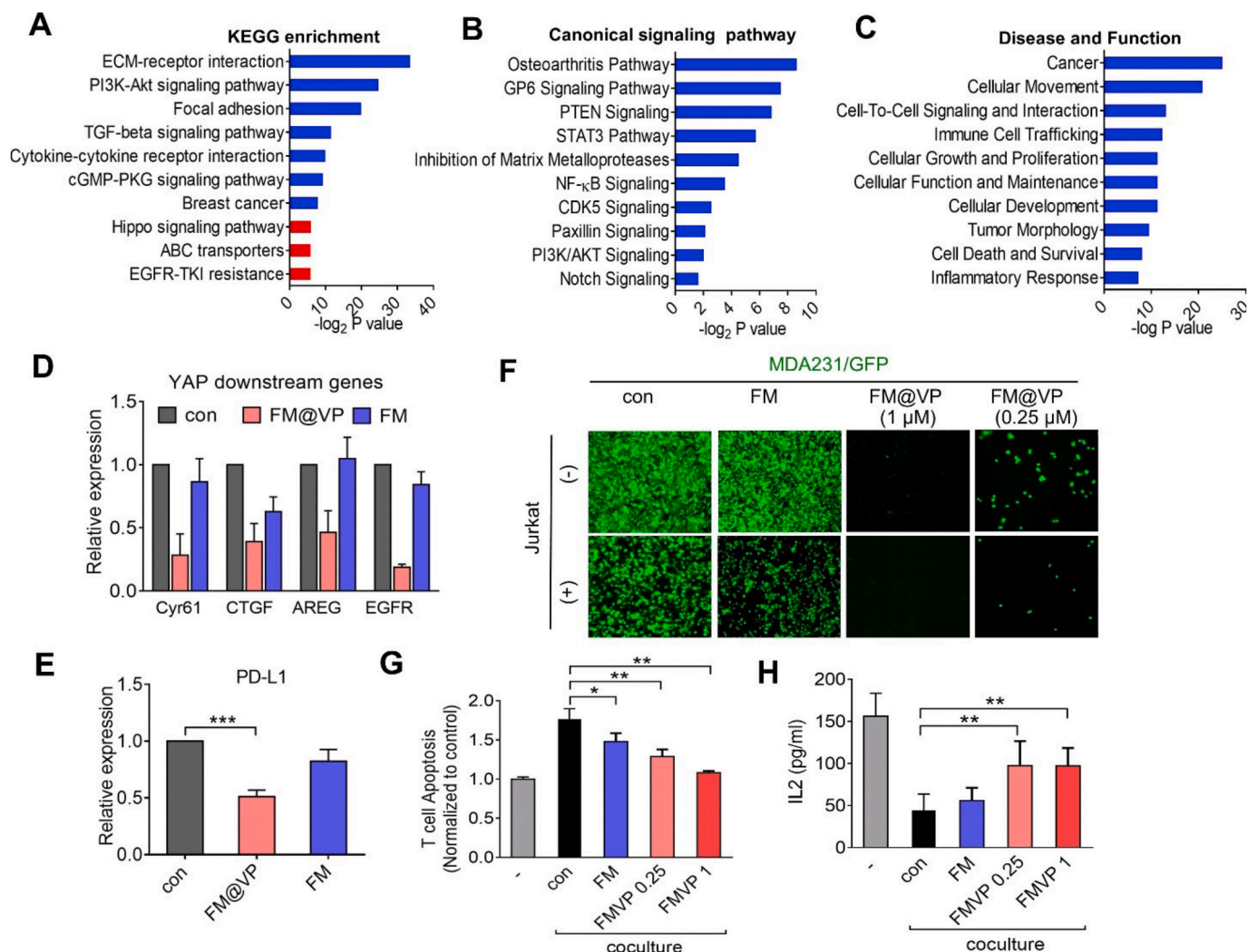


Fig. 4. Suppression of oncogenic signaling and PD-L1 expression by FM@VP. (A) Functional annotation of FM@VP-downregulated signaling by a Kyoto Encyclopedia of Genes and Genomes (KEGG) analysis. Selected pathways are highlighted in red. (B) Selected significantly enriched canonical signaling pathways and (C) disease and function affected by FM@VP from an Ingenuity pathway analysis (IPA). Bars represent significance of gene enrichment for a given pathway on a $-\log_2(p)$ value scale. (D, E) qRT-PCR analyses of YAP downstream targets (D) and PD-L1 (E) in MDA-MB-231 cells treated with FM@VP (containing 1 μ M VP) or FM nanoformulations. (F) Effect of FM@VP nanoparticles on a Jurkat T cell-elicited tumor-killing assay. MDA-MB-231/GFP cells were treated with FM@VP (containing 0.25 and 1 μ M VP) and FM nanocomplexes for 24 h, before being cocultured with activated Jurkat T cells. After 72 h of incubation, surviving tumor cells were observed under an inverted fluorescent microscope. (G, H) Measurements of T cell apoptosis (G) and interleukin (IL)-2 production (H) in a coculture of Jurkat T cells and FM nanoformulation-treated MDA-MB-231 cells, as described in “Materials and Methods”. Data are presented as the mean \pm SD. $^*p < 0.05$; $^{**}p < 0.01$; $^{***}p < 0.001$, assessed using an unpaired *t*-test. (For interpretation of the references to colour in this figure legend, the reader is referred to the Web version of this article.)

nanocomplex for 24 h followed by coculture with activated Jurkat T cells for another 48 h. We found that FM@VP with 1 μ M VP killed nearly all MDA-MB-231 cells, with or without T cell incubation (Fig. 4F, middle panel). Interestingly, pretreatment of MDA-MB-231 cells with an equivalent volume of FM had only modest inhibitory activity on tumor cells themselves, but it enhanced T cell-mediated cytotoxicity towards tumor cells (Fig. 4F, left panel). We also observed T cell-triggered shrinkage of MDA-MB-231 cells after pretreatment with FM nanocomplexes, compared to control MDA-MB-231 cells which exhibited mesenchymal features with a spindle-like structure (Supplemental Fig. S11). Importantly, treatment with a low concentration of FM@VP (encapsulating 0.25 μ M VP) enhanced T cell-mediated cytotoxicity (Fig. 4F, right panel). Because PD-L1/PD-1-mediated immune suppression is associated with reduced interleukin (IL)-2 production, which is a key cytokine for T cell proliferation and survival, we further measured IL-2 production by activated Jurkat T cells in coculture with MDA-MB-231 breast cancer cells. As shown in Fig. 4G and H, MDA-MB-231 cells were sufficient to suppress IL-2 production by T cells,

while this was reversed when MDA-MB-231 cells were pretreated with FM and FM@VP nanocomplexes. Notably, FM@VP encapsulating 0.25 μ M VP was capable of attenuating IL-2 production by T cells (Fig. 4G). Moreover, MDA-MB-231 cell-induced apoptosis of Jurkat T cells was blocked in the presence of FM and was also augmented in FM@VP nanoparticles (Fig. 4H). Together, these data indicate that the DFPN-based formulation possesses the ability to attenuate T cell-mediated cytotoxicity, while the encapsulation of VP boosts its antitumor immunity.

2.7. Targeted FM@VP for antitumor growth and antitumor metastasis

To verify the therapeutic activity of DFPN formulations against TNBC, we applied an orthotopic breast tumor model by implantation of 4T1 breast cancer cells into the mammary fat pad of BALB/c mice, and different DFPN formulations were intravenously injected via the tail vein followed by treatment with light irradiation for 30 min. Results showed that mice which received FM@VP nanoparticle clusters

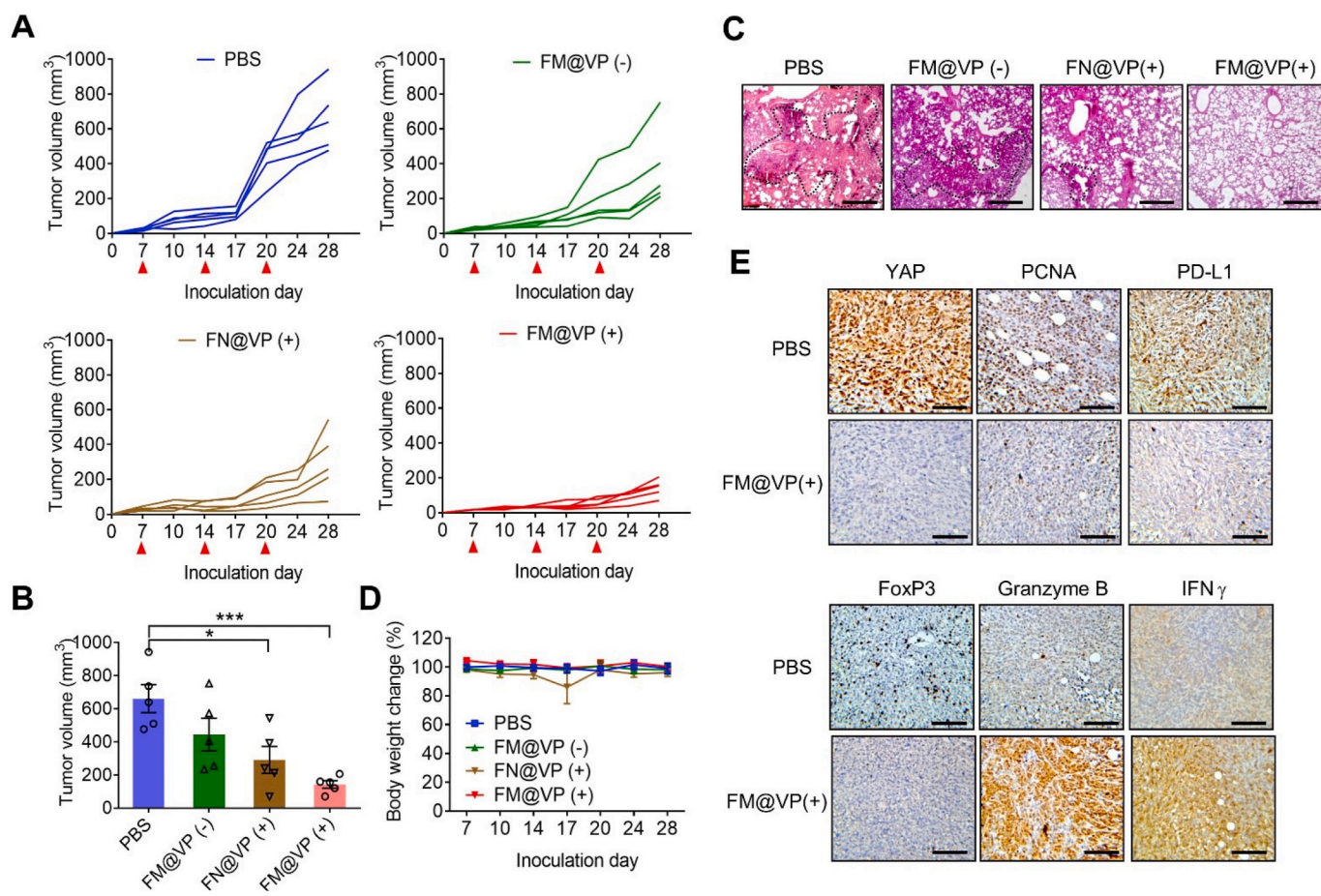


Fig. 5. FM@VP suppresses TNBC growth and metastasis. (A) Growth curve showing individual tumor volumes over time of 4T1 cells in BALB/c mice ($n = 5$) which were treated on days 7, 14, and 21 as indicated (red arrows). (B) Mean \pm SEM of tumor sizes at the end of the experiment. Significance was calculated using a one-way ANOVA and Holm-Sidak multiple comparison tests; $*p < 0.05$; $**p < 0.01$. (C) Histological analyses of spontaneous lung metastasis from orthotopically implanted 4T1 cells with different DFPN formulation treatments. Lung sections were stained with hematoxylin and eosin (H&E). Bar = 100 μ m. (D) Percentages of mice body weight changes. (E) Immunostaining of PBS and FM@VP(+)-exposed tumor tissues. Representative tumor tissues reacted with anti-YAP, PCNA, PD-L1, FoxP3 (Treg), Granzyme B, and IFN- γ antibodies. Scale bar = 200 μ m. (For interpretation of the references to colour in this figure legend, the reader is referred to the Web version of this article.)

encapsulating 1 mg/kg VP exhibited modestly reduced orthotopic tumor growth with a 32% reduction in tumor volume, compared to the control arm (Fig. 5A and B). Accordingly, mice treated with FN@VP plus light irradiation exhibited a 55% reduction in tumor growth (Fig. 5A and B). Notably, treatment of mice with FM@VP combined with light irradiation significantly suppressed orthotopic 4T1 cells by 78% (Fig. 5A and B). Importantly, we found that FM@VP combined with PDT drastically suppressed metastatic colonization of tumor cells in the lungs, compared to FN@VP plus phototherapy or FM@VP alone (Fig. 5C). These data indicate that FM@VP alone exhibited modest inhibitory activity against TNBC, whereas the combination of FM@VP and PDT displayed enhanced antitumor growth and metastasis. Additionally, no significant change in weight loss was seen after the treatment with different DFPN formulations (Fig. 5D), and no obvious lesions in the heart, kidneys, spleen, or liver were observed via histological analyses (Supplemental Fig. S12A), demonstrating the safety of using FM@VP for PDT. Moreover, the immunohistochemistry analysis showed that protein levels of YAP, proliferating cell nuclear antigen (PCNA; a proliferation marker), and PD-L1 were drastically decreased in FM@VP-treated tumor tissues (Fig. 5E upper panel). Besides, FM@VP treatment downregulated regulatory T (Treg) cell infiltration while it increased expressions of Granzyme B and gamma-interferon (IFN- γ) (Fig. 5E lower panel), indicating that FM@VP modulates immunosuppressive tumor microenvironment.

2.8. Targeted FM@VP activates antitumor immunity and enhances the abscopal effect

We further evaluated immunological profiles in the tumor and spleen of 4T1-bearing BALB/c mice after treatment with DFPN formulations. Results of flow cytometric analyses revealed that both CD3⁺CD4⁺ and CD3⁺CD8⁺ tumor-infiltrating T cells had increased across the different therapies. Of note, FM@VP combined with light irradiation substantially upregulated tumor-infiltrating T cells, compared to other treatments (Fig. 6A, Supplemental Fig. S13). Additionally, the population of CD11b + F4/80+ tumor-associated macrophages (TAMs) drastically decreased in response to FM nanoformulations (Fig. 6A, Supplemental Fig. S13), and FM@VP plus light irradiation significantly reduced infiltration of TAMs in tumor tissues (Fig. 6A, Supplemental Fig. S13). Similar results were obtained in spleen extracts with percentages of CD4 and CD8 T cells increasing, whereas the percentage of TAMs declined after treatment with FM@VP combined with phototherapy (Fig. 6B). Additionally, the expression of Granzyme B and IFN- γ were upregulated in FM@VP-treated spleen tissues (Supplemental Fig. S12B), suggesting the enhanced systemic immune response in FM@VP combined with phototherapy for completely enforcing the antitumor efficacy.

To further explore the abscopal effect due to FM@VP-mediated immunomodulation, a mouse TNBC model was evaluated by orthotopically injecting 4T1 cells into the left mammary fat pad (designated as the primary tumor), and then 4T1-Luc cells were injected into the

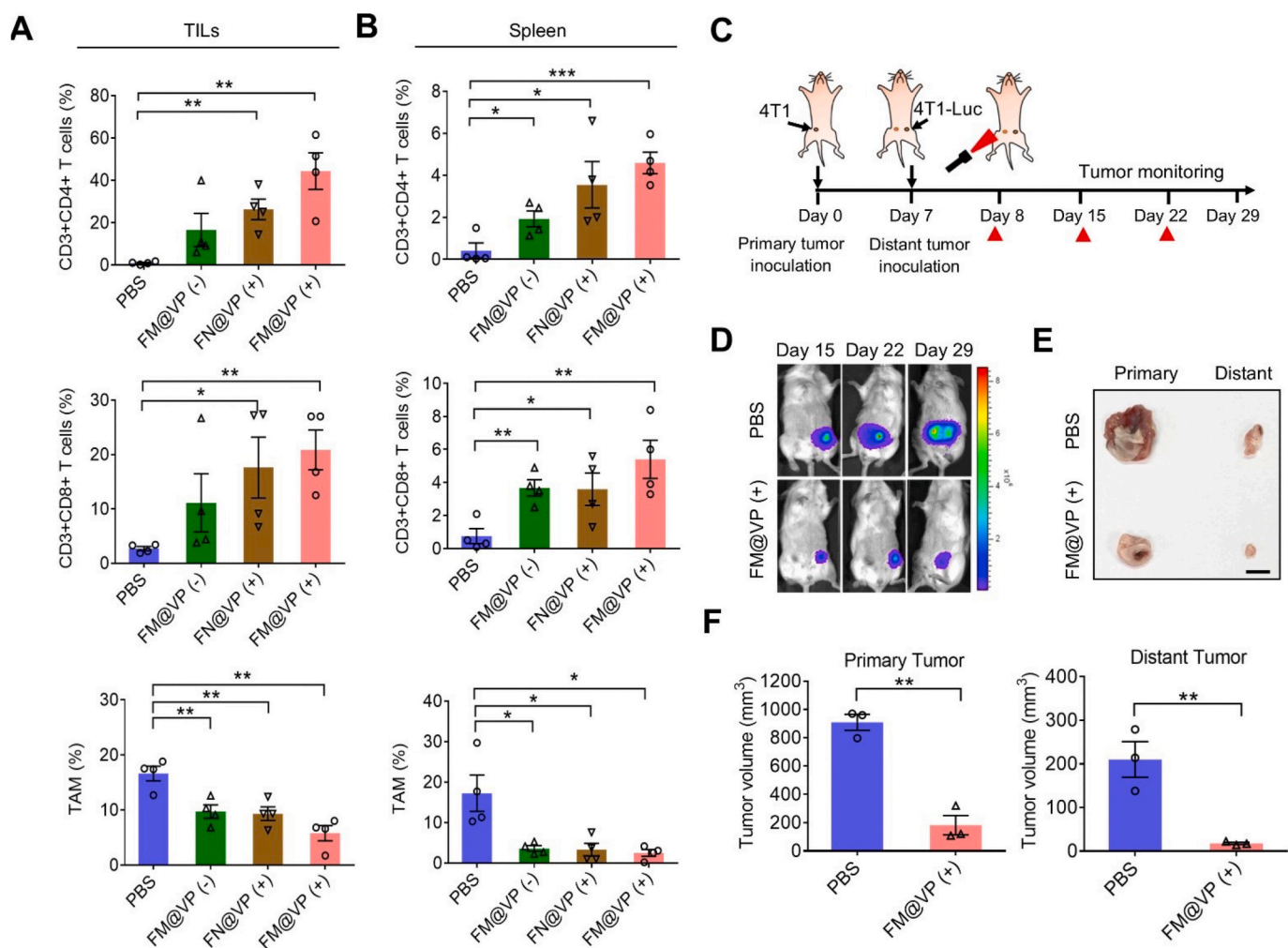


Fig. 6. FM@VP activates antitumor immunity and induces an abscopal effect. (A, B) Percentages of CD3⁺CD8⁺ and CD3⁺CD4⁺ T cells, and tumor-associated macrophages (TAMs) in the tumor (A) and spleen (B) of 4T1 cell-bearing BALB/c mice treated with different DFNP nanoformulations. Significance was calculated using a one-way ANOVA and Holm-Sidak multiple comparison tests; * $p < 0.05$; ** $p < 0.01$; *** $p < 0.001$ (C) Scheme for treatments and analyses. The secondary tumor was implanted in 4T1 cell-bearing mice after 7 days of inoculation followed by an orthotopic injection with 4T1-Luc cells into the bilateral site. Mice were administrated PBS and FM@VP, and the primary tumor received PDT (red arrows), with the rest of the body shielded. (D) IVIS bioluminescence images of distant tumor formation on days 15, 22, and 29. (E) Representative images of dissected tumor tissues at the end of the experiment. Scale bar = 1 cm. (F) Box plots of tumor volumes in primary and distant tumors on day 29. ** $p < 0.01$ assessed using an unpaired *t*-test. (For interpretation of the references to colour in this figure legend, the reader is referred to the Web version of this article.)

bilateral site 1 week after primary tumor inoculation (designated as the distant tumor). Then, the mice were intravenously administered FM@VP and shielded from light irradiation except for the primary tumor site (Fig. 6C). Results showed that the luminescent signal was detected and gradually increased in PBS group (Fig. 6D), whereas it was suppressed in the group treated with FM@VP plus PDT (Fig. 6D). Measurement of the tumor volume showed that the primary tumor was eradicated by FM@VP combined with phototherapy (Fig. 6E and F). Importantly, treating the primary tumor with FM@VP and PDT induced an abscopal effect on the distant tumor site (Fig. 6E and F).

Tumor escape from immune surveillance contributes to cancer development and drug resistance. One of these complicated mechanisms involves immune checkpoints. In view of this, immune checkpoint blockade was intensively evaluated in various malignancies, particularly in TNBC due to its relatively high level of PD-L1 [50,51]. Recently, there has been increased research illustrating the advantage of utilizing nanomedicine to overcome tumor-mediated immunosuppression, induce immune responses against tumor cells, and even activate memory immune cells [52,53]. Despite the induction of damaged signals having been described as eliciting activation of antitumor immunity by

PDT, the presence of immune checkpoints may dampen enthusiasm for and the effect of nanomedicines. Thus, the combination or conjugation with anti-PD-L1 drugs was exploited on various nanoplatfoms and showed efficiency, including with PDT [15,54,55]. However, the low synthetic rate and low selectivity may reduce the therapeutic efficacy and feasibility. In the present study, we showed that VP, an FDA-approved photosensitizer, not only acted as a PDT inducer but also inhibited expression of PD-L1 through suppressing YAP-regulated oncogenic signaling. We previously reported that overexpression of YAP was associated with drug resistance in breast cancer cells and unfavorable outcomes in TNBC patients [46]. YAP also participates in regulatory T (Treg) cell-mediated immune evasion [48]. Herein, we validated that FM@VP attenuated mitogenic signaling pathways, including PI3K-AKT, TGF- β , and Hippo, and FM@VP affected genes associated with cellular movement, growth, and differentiation. Our data also showed that FM@VP treatment downregulated PD-L1 and FoxP3 in tumor tissues, suggesting that downregulation of YAP by FM@VP may modulate immunosuppressive microenvironment. Moreover, FM@VP also enhanced systemic antitumor immune response as determined by the increase of Granzyme B and IFN γ in both tumor and

spleen tissues. Additionally, our previous study showed that inhibition of YAP decreased GSH level while increased oxidative GSSG level [45], suggesting that targeting YAP signaling by FM@VP might reduce GSH content and thereby increasing efficacy for PDT. Despite the *in vivo* study showing that treatment with FM@VP alone had only a minor inhibitory effect on tumor growth, it did modulate tumor immunity and enhanced the efficacy of PDT. As a results, FM@VP nanocomplexes efficiently suppressed tumor growth and metastasis, and induced an abscopal effect.

3. Conclusion

In summary, fucoidan-dendrimer-based FM@VP nanoplateform exhibits therapeutic advantages including (1) specificity towards P-selectin/YAP/PD-L1-overexpressing TNBC, (2) synergetic photodynamic/cancer-targeted therapy, and (3) an immunomodulatory capacity. It is a safe, biocompatible, and multifunctional nanoplateform to be a compelling therapeutic strategy for cancer treatment.

4. Experimental section

Synthesis of low-molecular weight fucoidan (LMWF): Fucoidan (*Laminaria japonica* fucoidan, 22% L-fucose and 34% sulfate) was purchased from NOVA Pharma & Liposome Biotech. LMWF was prepared according to a method reported in our previous study with a slight modification [56]. The fucoidan aqueous solution (10 mg/mL, 50 mL) was depolymerized with 0.1 M hydrogen peroxide (H₂O₂) under magnetic stirring at 70 °C for 1 h. The reaction was terminated by adding 0.1 M sodium carbonate. LMWF was then purified by ultrafiltration and dialysis with dialysis tubing (with a molecular weight cutoff of 1000 Da). The MW of the depolymerized product was determined by gel permeation chromatography (GPC) using a TSKgel G3000PWXL column (Tokyo, Japan) and a refractive index (RI) detector. An Na₂SO₄ aqueous solution (0.2 M) was used as the mobile phase, the flow rate was 0.5 mL/min, and the column temperature was 40 °C. Standard curves were constructed using dextran standards of different MWs (PSS Polymer Standards Service, Mainz, Germany).

Preparation of FM@VP: The detailed methodology for the synthesis and structure identification of the dendrimer is provided in "Supplemental Materials and Methods". To prepare MnO₂ NPs, a KMnO₄ solution (3 mg/mL) was mixed with a poly(allylamine hydrochloride) (PAH) solution (37.4 mg/mL; Alfa Aesar) at 9:1 v/v and stirred for 2 h to until the solution turned brown. The MnO₂ nanoparticles were purified by dialysis in deionized water for 24 h. VP (SelleckChem) was dissolved in dimethyl sulfoxide (DMSO). To assemble FM@VP nanoclusters, the fucoidan-VP mixture was prepared by adding VP (10 µg) into a 0.5% fucoidan solution (400 µL). Meanwhile, 0.25% dendrimer (80 µL) was mixed with 5 µL MnO₂ NPs. The dendrimer-MnO₂ mixture was carefully added into the fucoidan-VP mixture and stirred for a further 30 s to produce a colloidal solution. The final FM@VP nanoclusters product was centrifuged at 6000 rpm for 30 min to remove DMSO, and unencapsulated VP and MnO₂ NPs in supernatant. The centrifuged nanoclusters were washed with DI water and then were resuspended in PBS and used in further studies.

Characterization of FM@VP: The size distribution and zeta potential of DFPN formulations were measured with a Zetasizer Nano (Malvern Instruments, Malvern, UK). The morphology of FM@VP NP clusters was obtained by transmission electron microscopy (HT7700, Hitachi, Tokyo, Japan). Characteristics of fucoidan, VP, DFPN, and FM@VP were determined by Fourier transform infrared spectroscopy (FTIS; Frontier, PerkinElmer). Stability testing of the FM@VP, FN@VP and FM nanoformulations was performed by dispersing the nanoclusters in water, Dulbecco's modified Eagle medium (DMEM) (containing 7% fetal bovine serum; FBS), or a DTT solution. The mean particle size and polydispersity index (PDI) of the nanoformulations were analyzed with a Zetasizer Nano. To evaluate the loading efficacy of VP, FM@VP NPs

were centrifuged at 10,000 rpm for 10 min, and then the concentration of VP in the supernatant was determined by measuring the absorbance at 700 nm on a Spark M10 plate reader (Tecan Group) to evaluate the unencapsulated drug. The encapsulation efficiency was obtained according to the following formula: Encapsulation efficiency = (amount of drug contained in NPs/total dose of input) × 100%.

Detection of H₂O₂ decomposition and oxygen generation: PBS (100 µL) and FM (8 µg/µL, 50 µL) were respectively added in 96-well plate with and without the presence of H₂O₂ (3.0 wt%). The generation of O₂ was monitored by adding an oxygen sensing probe [(Ru(dpp)₃)]Cl₂ (10 µg/mL, 90 µL) to the samples and then the mixture were incubated at 37 °C for 30 min. The fluorescent intensity at 620 nm was recorded after excitation at 488 nm by a microplate reader (Infinite M200 pro, Tecan, Switzerland). The decomposition rate of H₂O₂ was determined by adding a H₂O₂ sensing kit (ferric-xylenol orange complex) to the samples followed by measuring the absorbance of the mixture at 560 nm.

Release of VP and MnO₂ NPs: Release of VP and MnO₂ NPs from FM@VP NPs clusters was investigated in PBS (pH 7.4) with and without DTT (500 mM) at 37 °C. The release media were withdrawn at pre-determined time intervals and then were centrifuged at 12,000 × g for 30 min to remove FM@VP NPs clusters. The supernatants were collected for analysis of the concentrations of VP and MnO₂ NPs. The release rate of VP was determined by measuring the absorbance at 700 nm on a Spark M10 plate reader (Tecan Group). The release rate of MnO₂ NPs was analyzed using inductively coupled plasma optical emission spectroscopy (ICP-OES, PerkinElmer Optima 200DV). Sigma-Aldrich).

Detection of ¹O₂ generation: The ¹O₂ generation was measured using singlet oxygen sensor green (SOSG). Briefly, PBS (100 µL) and FM, FM@VP and FN@VP (100 µL) nanoformulations were respectively added in 96-well plate with and without the presence of H₂O₂ (3.0 wt%), followed by light irradiation with 660 nm LED. The generated ¹O₂ was determined immediately by detecting the restored SOSG fluorescence.

Cellular uptake of FM@VP and competition assays: Mouse fibroblast 3T3-L1 and human TNBC MDA-MB-231 cells were cultured in DMEM supplemented with 7% FBS (Hyclone) and 1% penicillin/streptomycin with 5% CO₂ at 37 °C. Cells were seeded in a 24-well plate at a density of 5 × 10⁴ cells/well and treated with 1 µM VP and the FM@VP nanocomplex for 0–30 min. Additionally, MDA-MB-231 cells were pretreated with a 0.5% fucoidan solution followed by the addition of FM@VP for 30 min. Visualization of VP fluorescence was performed under a deconvolution fluorescent microscope (DeltaVision, GE Healthcare) at an excitation (Ex) frequency of 490 nm/emission (Em) frequency of 670 nm. To quantify the fluorescent intensity of VP, cells were washed with phosphate-buffered saline (PBS) and lysed with 1% Triton X-100. Cell lysates were centrifuged at 10,000 rpm for 30 min, and the supernatants were collected. The fluorescent intensity of VP in the supernatant was measured at Ex 420 nm/Em 690 nm on a Spark M10 plate reader (Tecan Group Ltd.).

Animal model: All animal models were carried out based on institutional guidelines and were approved by the Animal Care and Use Committee of Taipei Medical University. Female 8-week-old BALB/c mice (National Laboratory Animal Center, Taiwan) were inoculated on the left mammary fat pad with 10⁵ murine breast cancer 4T1 cells suspended in serum-free DMEM and Matrigel for 7 days. Mice were randomly divided into individual groups and intravenously injected with PBS, FM@VP (1 mg/kg), and FN@VP (1 mg/kg) with or without PDT treatment (1.1 W/cm², 690 nm). PDT was performed at 30 min post-injection and illuminated for 10 min for 3 consecutive days. The tumor size was calculated based on the equation: (width) × (length)²/2. At day 28 after tumor inoculation, the mice were sacrificed, and the heart, lungs, spleen, kidneys, and tumor were harvested for histological examination.

To evaluate the abscopal effect, a distant tumor was created in 4T1 cell-bearing mice 7 days after inoculation followed by an orthotopic injection with 10⁵ 4T1-Luc cells in the right mammary fat pad. Mice were randomly divided into two groups (n = 5) and intravenously

injected with PBS and FM@VP for 30 min. Mice were shielded from light except for the primary tumor site which received PDT for 10 min for 3 consecutive days. The formation of distant tumors was detected using IVIS bioluminescence system.

Statistical analysis: Each experiment was performed in triplicate, and results are expressed as the mean \pm standard deviation (SD) unless otherwise specifically indicated. The significance of the difference from the respective controls for each experimental test condition was assayed using an unpaired *t*-test. **p* < 0.05, ***p* < 0.01, and ****p* < 0.001 were regarded as a significant difference compared to the indicated group. Statistical analysis was carried out using GraphPad Prism software.

The detailed methodologies for cytotoxicity and phototoxicity assay, tube formation and transwell migration, isolation and analysis of tumor-infiltrating lymphocytes (TILs) and splenocytes, Western blot, T cell-mediated cytotoxic assay, 3D tumorsphere formation and hypoxia detection, 3D tumorsphere and tumor-associated vasculature formation assay, and histological analyses are provided in Supplemental Materials and Methods 2.

Declaration of competing interest

The authors declare that they have no known competing financial interests or personal relationships that could have appeared to influence the work reported in this paper.

CRediT authorship contribution statement

Chu-Hung Chung: Conceptualization, Methodology, Validation, Formal analysis, Investigation, Data curation, Visualization, Writing - original draft, Writing - review & editing. **Kun-Ying Lu:** Conceptualization, Investigation. **Wen-Jing Hsu:** Methodology, Validation, Formal analysis, Investigation. **Wen-Fu Lee:** Methodology, Formal analysis. **Jia-Zih Dai:** Methodology, Investigation, Formal analysis. **Pei-Wei Shueng:** Resources, Funding acquisition. **Cheng-Wei Lin:** Conceptualization, Methodology, Validation, Writing - review & editing, Supervision, Project administration, Funding acquisition. **Fwu-Long Mi:** Conceptualization, Methodology, Formal analysis, Visualization, Writing - original draft, Writing - review & editing, Supervision, Project administration, Funding acquisition.

Acknowledgements

This study was supported by grants from the Ministry of Science and Technology (MOST106-2320-B-038-040 and MOST107-2320-B-038-052-MY3 to CW Lin, and MOST101-2221-E-038-016-MY3 to FL Mi) and Far Eastern Memorial Hospital (FEMH-2019-C-013, FEMH-2020-C-041 to PW Shueng). The authors would like to acknowledge the Laboratory Animal Center at TMU for technical support.

Appendix A. Supplementary data

Supplementary data to this article can be found online at <https://doi.org/10.1016/j.biomaterials.2020.120227>.

Author contributions

CHC, KYL, WCL, WJH, WFL, JZD, and PWS performed experiments. CHC collected the data. CHC, KYL, WCL, WJH, CWL, and FLM designed the study and analyzed the data. CWL and FLM drafted, edited and revised the manuscript. All authors reviewed and approved the manuscript.

References

- [1] A.C. Garrido-Castro, N.U. Lin, K. Polyak, Insights into molecular classifications of triple-negative breast cancer: improving patient selection for treatment, *Canc. Discov.* 9 (2) (2019) 176–198.
- [2] A.P. Castano, P. Mroz, M.R. Hamblin, Photodynamic therapy and anti-tumour immunity, *Nat. Rev. Canc.* 6 (7) (2006) 535–545.
- [3] D.E. Dolmans, D. Fukumura, R.K. Jain, Photodynamic therapy for cancer, *Nat. Rev. Canc.* 3 (5) (2003) 380–387.
- [4] X. Li, N. Kwon, T. Guo, Z. Liu, J. Yoon, Innovative strategies for hypoxic-tumor photodynamic therapy, *Angew Chem. Int. Ed. Engl.* 57 (36) (2018) 11522–11531.
- [5] R. Jahanban-Esfahlan, M. de la Guardia, D. Ahmadi, B. Yousefi, Modulating tumor hypoxia by nanomedicine for effective cancer therapy, *J. Cell. Physiol.* 233 (3) (2018) 2019–2031.
- [6] P. Agostinis, K. Berg, K.A. Gengel, T.H. Foster, A.W. Girotti, S.O. Gollnick, S. M. Hahn, M.R. Hamblin, A. Juzeniene, D. Kessel, M. Korbelik, J. Moan, P. Mroz, D. Nowis, J. Piette, B.C. Wilson, J. Golab, Photodynamic therapy of cancer: an update, *Ca - Cancer J. Clin.* 61 (4) (2011) 250–281.
- [7] R. Liang, L. Liu, H. He, Z. Chen, Z. Han, Z. Luo, Z. Wu, M. Zheng, Y. Ma, L. Cai, Oxygen-boosted immunogenic photodynamic therapy with gold nanocages@ manganese dioxide to inhibit tumor growth and metastases, *Biomaterials* 177 (2018) 149–160.
- [8] T. Lin, X. Zhao, S. Zhao, H. Yu, W. Cao, W. Chen, H. Wei, H. Guo, O₂-generating MnO₂ nanoparticles for enhanced photodynamic therapy of bladder cancer by ameliorating hypoxia, *Theranostics* 8 (4) (2018) 990–1004.
- [9] L. Xing, J.H. Gong, Y. Wang, Y. Zhu, Z.J. Huang, J. Zhao, F. Li, J.H. Wang, H. Wen, H.L. Jiang, Hypoxia alleviation-triggered enhanced photodynamic therapy in combination with Ido inhibitor for preferable cancer therapy, *Biomaterials* 206 (2019) 170–182.
- [10] Z. Chen, L. Liu, R. Liang, Z. Luo, H. He, Z. Wu, H. Tian, M. Zheng, Y. Ma, L. Cai, Bioinspired hybrid protein oxygen nanocarrier amplified photodynamic therapy for eliciting anti-tumor immunity and abscopal effect, *ACS Nano* 12 (8) (2018) 8633–8645.
- [11] S.L. Cramer, A. Saha, J. Liu, S. Tadi, S. Tiziani, W. Yan, K. Triplett, C. Lamb, S. E. Alters, S. Rowlinson, Y.J. Zhang, M.J. Keating, P. Huang, J. DiGiovanni, G. Georgiou, E. Stone, Systemic depletion of L-cyst(e)ine with cyst(e)inase increases reactive oxygen species and suppresses tumor growth, *Nat. Med.* 23 (1) (2017) 120–127.
- [12] W. Zhang, J. Lu, X. Gao, P. Li, W. Zhang, Y. Ma, H. Wang, B. Tang, Enhanced photodynamic therapy by reduced levels of intracellular glutathione obtained by employing a nano-MOF with Cu(II) as the active center, *Angew Chem. Int. Ed. Engl.* 57 (18) (2018) 4891–4896.
- [13] W. Yang, F. Zhang, H. Deng, L. Lin, S. Wang, F. Kang, G. Yu, J. Lau, R. Tian, M. Zhang, Z. Wang, L. He, Y. Ma, G. Niu, S. Hu, X. Chen, Smart nanovesicle-mediated immunogenic cell death through tumor microenvironment modulation for effective photodynamic immunotherapy, *ACS Nano* 14 (1) (2020) 620–631.
- [14] H. Deng, Z. Zhou, W. Yang, L.S. Lin, S. Wang, G. Niu, J. Song, X. Chen, Endoplasmic reticulum targeting to amplify immunogenic cell death for cancer immunotherapy, *Nano Lett.* 20 (3) (2020) 1928–1933.
- [15] X. Duan, C. Chan, N. Guo, W. Han, R.R. Weichselbaum, W. Lin, Photodynamic therapy mediated by nontoxic core-shell nanoparticles synergizes with immune checkpoint blockade to elicit antitumor immunity and antimetastatic effect on breast cancer, *J. Am. Chem. Soc.* 138 (51) (2016) 16686–16695.
- [16] D.J. Irvine, E.L. Dane, Enhancing cancer immunotherapy with nanomedicine, *Nat. Rev. Immunol.* 20 (5) (2020) 321–334.
- [17] S. Yan, X. Zeng, Y. Tang, B.F. Liu, Y. Wang, X. Liu, Activating antitumor immunity and antimetastatic effect through polydopamine-encapsulated core-shell upconversion nanoparticles, *Adv. Mater.* 31 (46) (2019), e1905825.
- [18] J. Xu, L. Xu, C. Wang, R. Yang, Q. Zhuang, X. Han, Z. Dong, W. Zhu, R. Peng, Z. Liu, Near-infrared-triggered photodynamic therapy with multitasking upconversion nanoparticles in combination with checkpoint blockade for immunotherapy of colorectal cancer, *ACS Nano* 11 (5) (2017) 4463–4474.
- [19] C.S. Chiang, Y.J. Lin, R. Lee, Y.H. Lai, H.W. Cheng, C.H. Hsieh, W.C. Shyu, S. Y. Chen, Combination of fucoidan-based magnetic nanoparticles and immunomodulators enhances tumour-localized immunotherapy, *Nat. Nanotechnol.* 13 (8) (2018) 746–754.
- [20] L. Chen, L. Zhou, C. Wang, Y. Han, Y. Lu, J. Liu, X. Hu, T. Yao, Y. Lin, S. Liang, S. Shi, C. Dong, Tumor-targeted drug and CpG delivery system for phototherapy and docetaxel-enhanced immunotherapy with polarization toward M1-type macrophages on triple negative breast cancers, *Adv. Mater.* 31 (52) (2019), e1904997.
- [21] Q. Li, D. Zhang, J. Zhang, Y. Jiang, A. Song, Z. Li, Y. Luan, A three-in-one immunotherapy nanoweapon via cascade-amplifying cancer-immunity cycle against tumor metastasis, relapse, and postsurgical regrowth, *Nano Lett.* 19 (9) (2019) 6647–6657.
- [22] J.K. Stolarczyk, A. Deak, D.F. Brougham, Nanoparticle clusters: assembly and control over internal order, current capabilities, and future potential, *Adv. Mater.* 28 (27) (2016) 5400–5424.
- [23] K. Yamamoto, T. Imaoka, M. Tanabe, T. Kambe, New horizon of nanoparticle and cluster catalysis with dendrimers, *Chem. Rev.* 120 (2) (2020) 1397–1437.
- [24] R. Ye, A.V. Zhukhovitskiy, C.V. Deraedt, F.D. Toste, G.A. Somorjai, Supported dendrimer-encapsulated metal clusters: toward heterogenizing homogeneous catalysts, *Acc. Chem. Res.* 50 (8) (2017) 1894–1901.
- [25] L. Grana-Suarez, W. Verboom, R.J.M. Egberink, S. Sarkar, V. Mahalingam, J. Huskens, Host-guest and electrostatic interactions in supramolecular nanoparticle clusters, *Eur. J. Org. Chem.* 2016 (33) (2016) 5511–5518.

- [26] Y. Shamay, M. Elkabets, H. Li, J. Shah, S. Brook, F. Wang, K. Adler, E. Baut, M. Scaltriti, P.V. Jena, E.E. Gardner, J.T. Poirier, C.M. Rudin, J. Baselga, A. Haimovitz-Friedman, D.A. Heller, P-selectin is a nanotherapeutic delivery target in the tumor microenvironment, *Sci. Transl. Med.* 8 (345) (2016), 345ra87.
- [27] A.K. Sharma, A. Gothwal, P. Kesharwani, H. Alsaab, A.K. Iyer, U. Gupta, Dendrimer nanoarchitectures for cancer diagnosis and anticancer drug delivery, *Drug Discov. Today* 22 (2) (2017) 314–326.
- [28] K.Y. Lu, R. Li, C.H. Hsu, C.W. Lin, S.C. Chou, M.L. Tsai, F.L. Mi, Development of a new type of multifunctional fucoidan-based nanoparticles for anticancer drug delivery, *Carbohydr. Polym.* 165 (2017) 410–420.
- [29] L.C. Tsai, C.H. Chen, C.W. Lin, Y.C. Ho, F.L. Mi, Development of multifunctional nanoparticles self-assembled from trimethyl chitosan and fucoidan for enhanced oral delivery of insulin, *Int. J. Biol. Macromol.* 126 (2019) 141–150.
- [30] C.H. Chen, Y.S. Lin, S.J. Wu, F.L. Mi, Multifunctional nanoparticles prepared from arginine-modified chitosan and thiolated fucoidan for oral delivery of hydrophobic and hydrophilic drugs, *Carbohydr. Polym.* 193 (2018) 163–172.
- [31] S.H. Yu, D.W. Tang, H.Y. Hsieh, W.S. Wu, B.X. Lin, E.Y. Chuang, H.W. Sung, F. L. Mi, Nanoparticle-induced tight-junction opening for the transport of an anti-angiogenic sulfated polysaccharide across Caco-2 cell monolayers, *Acta Biomater.* 9 (7) (2013) 7449–7459.
- [32] S.H. Yu, S.J. Wu, J.Y. Wu, D.Y. Wen, F.L. Mi, Preparation of fucoidan-shelled and genipin-crosslinked chitosan beads for antibacterial application, *Carbohydr. Polym.* 126 (2015) 97–107.
- [33] T.W. Huang, Y.C. Ho, T.N. Tsai, C.L. Tseng, F.L. Mi, Enhancement of the permeability and activities of epigallocatechin gallate by quaternary ammonium chitosan/fucoidan nanoparticles, *Carbohydr. Polym.* (2020) 116312.
- [34] T.M. Cheng, R. Li, Y.C. Jill Kao, C.H. Hsu, H.L. Chu, K.Y. Lu, C.A. Changou, C. C. Chang, L.H. Chang, M.L. Tsai, F.L. Mi, Synthesis and characterization of Gd-DTPA/fucoidan/peptide complex nanoparticle and in vitro magnetic resonance imaging of inflamed endothelial cells, *Mater. Sci. Eng. C* (2020) 111064.
- [35] W. She, N. Li, K. Luo, C. Guo, G. Wang, Y. Geng, Z. Gu, Dendronized heparin-doxorubicin conjugate based nanoparticle as pH-responsive drug delivery system for cancer therapy, *Biomaterials* 34 (9) (2013) 2252–2264.
- [36] M. Huo, W. Li, A.S. Chaudhuri, Y. Fan, X. Han, C. Yang, Z. Wu, X. Qi, Bio-stimuli-responsive multi-scale hyaluronic acid nanoparticles for deepened tumor penetration and enhanced therapy, *Carbohydr. Polym.* 171 (2017) 173–182.
- [37] D.G. He, L. Hai, X. He, X. Yang, H.W. Li, Glutathione-activatable and O-2/Mn2+-evolving nanocomposite for highly efficient and selective photodynamic and gene-silencing dual therapy, *Adv. Funct. Mater.* 27 (46) (2017).
- [38] J. Zhang, M.Q. Xu, Y.L. Mu, J.J. Li, M.F. Foda, W.Y. Zhang, K. Han, H.Y. Han, Reasonably retard O-2 consumption through a photoactivity conversion nanocomposite for oxygenated photodynamic therapy, *Biomaterials* 218 (2019).
- [39] Q.Y. Tang, Z.J. Cheng, N. Yang, Q.Z. Li, P. Wang, D.P. Chen, W.J. Wang, X.J. Song, X.C. Dong, Hydrangea-structured tumor microenvironment responsive degradable nanopatform for hypoxic tumor multimodal imaging and therapy, *Biomaterials* 205 (2019) 1–10.
- [40] X. Zhang, Z.Q. Xi, J.O. Machuki, J.J. Luo, D.Z. Yang, J.J. Li, W.B. Cai, Y. Yang, L. J. Zhang, J.W. Tian, K.J. Guo, Y.Y. Yu, F.L. Gao, Gold cube-in-cube based oxygen nanogenerator: a theranostic nanopatform for modulating tumor microenvironment for precise chemo-phototherapy and multimodal imaging, *ACS Nano* 13 (5) (2019) 5306–5325.
- [41] A. Le, Z.E. Stine, C. Nguyen, J. Afzal, P. Sun, M. Hamaker, N.M. Siegel, A.M. Gouw, B.H. Kang, S.H. Yu, R.L. Cochran, K.A. Sailor, H. Song, C.V. Dang, Tumorigenicity of hypoxic respiring cancer cells revealed by a hypoxia-cell cycle dual reporter, *Proc. Natl. Acad. Sci. U. S. A.* 111 (34) (2014) 12486–12491.
- [42] W.J. Hsu, M.H. Lin, T.C. Kuo, C.M. Chou, F.L. Mi, C.H. Cheng, C.W. Lin, Fucoidan from *Laminaria japonica* exerts antitumor effects on angiogenesis and micrometastasis in triple-negative breast cancer cells, *Int. J. Biol. Macromol.* 149 (2020) 600–608.
- [43] L. Wu, J. Sun, X. Su, Q. Yu, Q. Yu, P. Zhang, A review about the development of fucoidan in antitumor activity: progress and challenges, *Carbohydr. Polym.* 154 (2016) 96–111.
- [44] W.Y. Lee, P.C. Chen, W.S. Wu, H.C. Wu, C.H. Lan, Y.H. Huang, C.H. Cheng, K. C. Chen, C.W. Lin, Panobinostat sensitizes KRAS-mutant non-small-cell lung cancer to gefitinib by targeting TAZ, *Int. J. Canc.* 141 (9) (2017) 1921–1931.
- [45] C.C. Kuo, H.H. Ling, M.C. Chiang, C.H. Chung, W.Y. Lee, C.Y. Chu, Y.C. Wu, C. H. Chen, Y.W. Lai, I.L. Tsai, C.H. Cheng, C.W. Lin, Metastatic colorectal cancer rewrites metabolic program through a glut3-YAP-dependent signaling circuit, *Theranostics* 9 (9) (2019) 2526–2540.
- [46] C.E. Yang, W.Y. Lee, H.W. Cheng, C.H. Chung, F.L. Mi, C.W. Lin, The antipsychotic chlorpromazine suppresses YAP signaling, stemness properties, and drug resistance in breast cancer cells, *Chem. Biol. Interact.* 302 (2019) 28–35.
- [47] H.J. Janse van Rensburg, T. Azad, M. Ling, Y. Hao, B. Snetsinger, P. Khanal, L. M. Minassian, C.H. Graham, M.J. Rauh, X. Yang, The Hippo pathway component TAZ promotes immune evasion in human cancer through PD-L1, *Canc. Res.* 78 (6) (2018) 1457–1470.
- [48] M.H. Kim, C.G. Kim, S.K. Kim, S.J. Shin, E.A. Choe, S.H. Park, E.C. Shin, J. Kim, YAP-induced PD-L1 expression drives immune evasion in BRAFi-resistant melanoma, *Cancer Immunol Res* 6 (3) (2018) 255–266.
- [49] M. Nishino, N.H. Ramaiya, H. Hatabu, F.S. Hodi, Monitoring immune-checkpoint blockade: response evaluation and biomarker development, *Nat. Rev. Clin. Oncol.* 14 (11) (2017) 655–668.
- [50] D. Romero, Benefit in patients with PD-L1-positive TNBC, *Nat. Rev. Clin. Oncol.* 16 (1) (2019) 6.
- [51] P. Schmid, S. Adams, H.S. Rugo, A. Schneeweiss, C.H. Barrios, H. Iwata, V. Dieras, R. Hegg, S.A. Im, G. Shaw Wright, V. Henschel, L. Molinero, S.Y. Chui, R. Funke, A. Husain, E.P. Winer, S. Loi, L.A. Emens, I.M.T. Investigators, Atezolizumab and nab-paclitaxel in advanced triple-negative breast cancer, *N. Engl. J. Med.* 379 (22) (2018) 2108–2121.
- [52] M.S. Goldberg, Improving cancer immunotherapy through nanotechnology, *Nat. Rev. Canc.* 19 (10) (2019) 587–602.
- [53] J.D. Martin, H. Cabral, T. Stylianopoulos, R.K. Jain, Improving cancer immunotherapy using nanomedicines: progress, opportunities and challenges, *Nat. Rev. Clin. Oncol.* 17 (4) (2020) 251–266.
- [54] R. Zhang, Z. Zhu, H. Lv, F. Li, S. Sun, J. Li, C.S. Lee, Immune checkpoint blockade mediated by a small-molecule nanoinhibitor targeting the PD-1/PD-L1 pathway synergizes with photodynamic therapy to elicit antitumor immunity and antimetastatic effects on breast cancer, *Small* 15 (49) (2019), e1903881.
- [55] L. Hu, Z. Cao, L. Ma, Z. Liu, G. Liao, J. Wang, S. Shen, D. Li, X. Yang, The potentiated checkpoint blockade immunotherapy by ROS-responsive nanocarrier-mediated cascade chemo-photodynamic therapy, *Biomaterials* 223 (2019) 119469.
- [56] Y.H. Lin, K.Y. Lu, C.L. Tseng, J.Y. Wu, C.H. Chen, F.L. Mi, Development of genipin-crosslinked fucoidan/chitosan-N-arginine nanogels for preventing Helicobacter infection, *Nanomedicine* 12 (12) (2017) 1491–1510.